

Research Article

A Three-Phase Bidirectional Grid-Connected AC/DC Converter for V2G Applications

Jingang Han , Xiong Zhou, Song Lu, and Pinxuan Zhao

Institute of Electric Drives and Control Systems, Shanghai Maritime University, Shanghai 201306, China

Correspondence should be addressed to Jingang Han; jghan@shmtu.edu.cn

Received 1 July 2020; Revised 14 August 2020; Accepted 25 August 2020; Published 7 September 2020

Academic Editor: Mohamedy Hamdy

Copyright © 2020 Jingang Han et al. This is an open access article distributed under the Creative Commons Attribution License, which permits unrestricted use, distribution, and reproduction in any medium, provided the original work is properly cited.

The smart grid and electric vehicles (EVs) are widely used all over the world. As the key role, the Vehicle-to-Grid (V2G) has been attracting increasing attention. The bidirectional grid-connected AC/DC converter is one of the indispensable parts in the V2G system, which can realize bidirectional power flow and meet the power quality requirements for grid. A three-phase bidirectional grid-connected AC/DC converter is presented in this paper for V2G systems. It can be used to achieve the bidirectional power flow between EVs and grid, supply reactive power compensation, and smooth the power grid fluctuation. Firstly, the configuration of V2G systems is introduced, and the mathematical model of the AC/DC converter is built. Then, for bidirectional AC/DC converters, the grid voltage feedforward decoupling scheme is applied, and the analysis of PI control strategy is proposed and the controller is designed. The system simulation model is established based on MATLAB/Simulink, and the experiment platform of the bidirectional grid-connected converter for V2G is designed in lab. The simulation and experiment results are shown, and the results evaluate the effectiveness of the model and the performance of the applied control strategy.

1. Introduction

Recently, with the environmental degradation, climate change, and the shortage of fossil energy, the traditional energy costs have risen a lot. Thus, it is urgent to use new and clean energy worldwide. Plug-in Electric Vehicles (PEVs) and Electric Vehicles (EVs) have attracted increasing attention worldwide [1–3], due to the representativeness of new energy vehicles. There are a lot of advantages about EVs and PEVs, such as peak power regulating, peak load shifting, environment protection, low cost, and so on. EVs and PEVs not only can be loads in grid-to-vehicle (G2V) charge mode but also can be generators in vehicle-to-grid (V2G) discharge mode [4]. Generally, both V2G and G2V applications are suitable for “V2G.”

The power converter is unidirectional for G2V in general, which includes conventional and fast charging system. Owing to the fact that the power of typical electrical vehicles is twice higher than the average household load, the grid network will be stressed by the

fast charging [5]. If the G2V charger does not employ the state-of-the-art conversion, this may lead to disturbances in grid, such as undesirable peak loads, harmonics, and low power factor [6, 7]. Thus, it is essential to support energy injection back to the grid in V2G system. Bidirectional grid-connected AC/DC converter is one of the indispensable parts in the V2G system, which can realize the sinusoidal input current and bidirectional power flow. For V2G applications, improving power density, reducing input and output current ripple, and having reactive power compensation capability are the major research directions for bidirectional AC/DC converter [8–10].

In recent years, there are different kinds of AC/DC converter topologies used in the V2G system, including single-stage single-phase and three-phase, two-stage single-phase and three-phase, ZVS inverter, and so on [11, 12]. Reference [13] presents an electrical vehicle charger that used a single-phase interleaved AC/DC boost converter. In [14], a high-performance single-phase bridgeless interleaved

PFC converter is proposed. Both [13, 14] have the same function, which can reduce the battery charge and discharge current ripple, however, neither of them could work with wide output voltage. In [15, 16], unidirectional buck-boost converters with wide output voltage are proposed, which can reduce the Total Harmonic Distortion (THD) of AC current. Because of the unidirectional switches, all these converters cannot feedback the battery energy to the grid. To realize the bidirectional power flow, the AC/DC matrix converters are proposed in [17]. However, the converter is known for its large amounts of semiconductor switches and high-frequency operation, which will lead to higher cost and larger losses including switching losses and conduction losses. In [18], a current-source rectifier is shown with an auxiliary switching network. The advantages of this converter are high efficiency and achieved the bidirectional power flow, but it will reduce the battery life owing to the input current ripple. The study in [19] proposed a current-source rectifier with PWM pulse signal trilogic control method. In [20, 21], the intelligence protection technique is proposed, which can be used in the high-power grid-connected converter. The authors of [22, 23] presented the maximum current control and grid voltage full-feedforward scheme for three-phase voltage-source rectifier.

There are several different disadvantages in the topologies mentioned above when used in V2G, such as the narrow output voltage range, large losses, and high input current ripple. As an effective alternative, a three-phase bidirectional grid-connected converter for V2G system is analyzed and designed in this paper, which realized bidirectional power flow, high efficiency, unity power factor, and wide battery pack voltage range. In Section 2, the system configuration is introduced, and the mathematical models of bidirectional AC/DC and DC/DC converter are built in detail. In Section 3, the control strategies, including the grid voltage feedforward decoupling scheme, and the double closed-loop control of AC/DC converter are analyzed and designed. In Section 4, the experimental prototype is built in lab; then, the simulation and experiment results are proposed and discussed. Finally, conclusions of this paper are in Section 5.

2. System Configuration and Model

2.1. System Configuration. The configuration of V2G system is shown in Figure 1; the system consists of three parts, AC grid, converters, and loads. AC grid supplies original AC voltage to converters through a transformer, of which the ratio is 380:480. Converters consist of AC/DC converter and DC/DC converter. The AC/DC converters transform AC energy to DC energy. The bidirectional DC/DC converter connects the battery to the DC bus. In this paper, charging the battery is defined as positive; on the contrary, discharging is defined as negative.

2.2. Modeling of Bidirectional AC/DC Converters. The topology of a three-phase voltage-source converter is shown in Figure 2. An L filter is used to connect to the grid and converter. The ideal AC grid source is denoted as e_a, e_b, e_c . And i_a, i_b, i_c denote the source current. L is the inductance filter, and R is the resistance of series R - L circuit. C is the DC-side capacitor. u_{dc} and i_{dc} are the DC-side voltage and current. A resistance R_L and e_L in series are equivalent to the DC load.

According to the KCL and KVL, the system model can be expressed as [22]

$$\begin{cases} e_a = L \frac{di_a}{dt} + Ri_a + u_{aN} + u_{NO}, \\ e_b = L \frac{di_b}{dt} + Ri_b + u_{bN} + u_{NO}, \\ e_c = L \frac{di_c}{dt} + Ri_c + u_{cN} + u_{NO}, \\ C \frac{du_{dc}}{dt} = i_{dc} - i_L, \end{cases} \quad (1)$$

where $u_{aN}, u_{bN},$ and u_{cN} are the voltage between the three converter legs midpoint and point N and u_{NO} is the voltage between point N and O .

When switches S_{a1}, S_{b1}, S_{c1} are on and switches S_{a2}, S_{b2}, S_{c2} are off, the switching function is $S_k = 1$. When switches S_{a2}, S_{b2}, S_{c2} are on and S_{a1}, S_{b1}, S_{c1} are off, the function is $S_k = 0$. Therefore, u_k can be defined as [22]

$$u_k = u_{kN} + u_{NO} = S_k u_{dc} + u_{NO}, \quad (k = a, b, c). \quad (2)$$

For a balanced three-phase system without the neutral line, the phase currents are $i_a + i_b + i_c = 0$ and phase voltages are $e_a + e_b + e_c = 0$. Equation (1) can be described as [22]

$$\begin{cases} e_a = L \frac{di_a}{dt} + Ri_a + u_{dc} \left[S_a - \frac{1}{3} (S_a + S_b + S_c) \right], \\ e_b = L \frac{di_b}{dt} + Ri_b + u_{dc} \left[S_b - \frac{1}{3} (S_a + S_b + S_c) \right], \\ e_c = L \frac{di_c}{dt} + Ri_c + u_{dc} \left[S_c - \frac{1}{3} (S_a + S_b + S_c) \right], \\ C \frac{du_{dc}}{dt} = i_a S_a + i_b S_b + i_c S_c - i_L. \end{cases} \quad (3)$$

Comparing to the $a-b-c$ frame, it is convenient to control the system in stationary $\alpha-\beta$ frame. The transformation and inverse transformation of the stationary $a-b-c$ frame to $\alpha-\beta$ frame used in this paper are defined as [23]

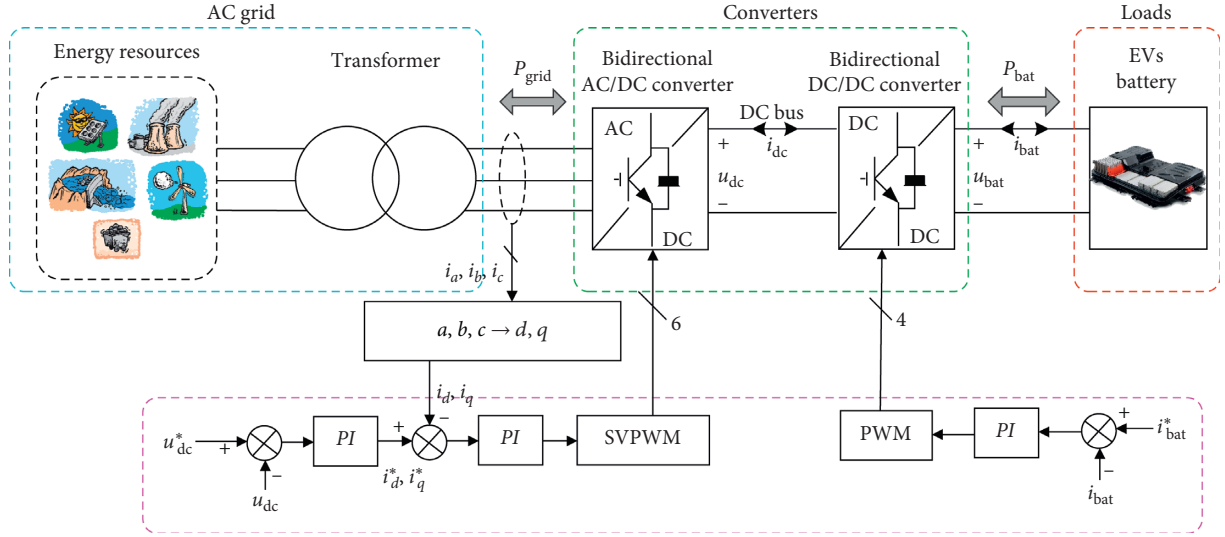


FIGURE 1: System configuration.

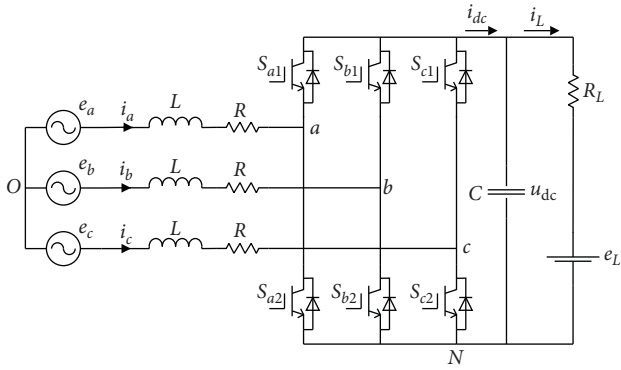


FIGURE 2: The circuit of bidirectional AC/DC converter.

$$\begin{bmatrix} x_\alpha \\ x_\beta \end{bmatrix} = [M] \begin{bmatrix} x_a \\ x_b \\ x_c \end{bmatrix}, \quad (4)$$

$$[M] = \frac{2}{3} \begin{bmatrix} 1 & \frac{1}{2} & \frac{1}{2} \\ 0 & \frac{\sqrt{3}}{2} & \frac{\sqrt{3}}{2} \end{bmatrix},$$

$$\begin{bmatrix} x_a \\ x_b \\ x_c \end{bmatrix} = \frac{3}{2} [M]^T \begin{bmatrix} x_\alpha \\ x_\beta \end{bmatrix}, \quad (5)$$

$$\frac{3}{2} [M]^T = \begin{bmatrix} 1 & 0 \\ \frac{1}{2} & \frac{\sqrt{3}}{2} \\ \frac{1}{2} & \frac{\sqrt{3}}{2} \end{bmatrix},$$

where x_α and x_β are the stationary $\alpha - \beta$ frame quantities and $x_a, x_b,$ and x_c are the quantities of stationary $a - b - c$ frame.

Applying (5) to transform (3), the converter model in $\alpha - \beta$ frame can be described as [23]

$$\begin{cases} e_\alpha = L \frac{di_\alpha}{dt} + Ri_\alpha + S_\alpha u_{dc}, \\ e_\beta = L \frac{di_\beta}{dt} + Ri_\beta + S_\beta u_{dc}, \\ C \frac{du_{dc}}{dt} = \frac{3}{2} (i_\alpha S_\alpha + i_\beta S_\beta) - i_L. \end{cases} \quad (6)$$

It is no surprise that the grid voltage and current in stationary $\alpha - \beta$ frame is sinusoidal time variable. In order to control the power flow conveniently, the synchronous $d - q$ frame control is employed. The transformation and its inverse transformation of frame $\alpha - \beta$ to synchronous $d - q$ frame is defined as [23]

$$\begin{bmatrix} x_d \\ x_q \end{bmatrix} = [T] \begin{bmatrix} x_\alpha \\ x_\beta \end{bmatrix}, \quad (7)$$

$$[T] = \begin{bmatrix} \cos(\omega_0 t) & \sin(\omega_0 t) \\ -\sin(\omega_0 t) & \cos(\omega_0 t) \end{bmatrix},$$

$$\begin{bmatrix} x_\alpha \\ x_\beta \end{bmatrix} = [T]^{-1} \begin{bmatrix} x_d \\ x_q \end{bmatrix}, \quad (8)$$

$$[T]^{-1} = \begin{bmatrix} \cos(\omega_0 t) & -\sin(\omega_0 t) \\ \sin(\omega_0 t) & \cos(\omega_0 t) \end{bmatrix},$$

where x_α and x_β are the stationary $\alpha - \beta$ frame quantities and x_d and x_q are the synchronous $d - q$ frame quantities.

Considering (7) and (6), the model can be described as [23]

$$\begin{cases} e_d = L \frac{di_d}{dt} + Ri_d - \omega_0 Li_q + S_d u_{dc}, \\ e_q = L \frac{di_q}{dt} + Ri_q + \omega_0 Li_d + S_q u_{dc}, \\ C \frac{du_{dc}}{dt} = \frac{3}{2} (i_d S_d + i_q S_q) - i_L. \end{cases} \quad (9)$$

According to (9), the mathematic model of three-phase voltage-source converter in synchronous $d-q$ frame is shown in Figure 3.

2.3. Modeling of Bidirectional DC/DC Converters. The topology of the bidirectional DC/DC converter is shown in Figure 4, which connects DC bus to battery pack. And the bidirectional H-bridge DC/DC converter will meet the wide voltage requirement of battery. The DC bus voltage of DC/DC converter is denoted as V_{bus} . The filter circuit consists of L_1 and C_0 .

The converter works in buck mode for charging the battery. On the contrary, the converter works in boost mode. Taking the buck mode as example, the control transfer function for the converter can be expressed as [24, 25]

$$G_{i_d}(s) = \frac{2V_{bus}(sC_0 + (1/R_{Load}))}{L_1 C_0 s^2 + (L_1/R_{Load})s + 1}. \quad (10)$$

Similarly, the control transfer function for the converter in boost mode can be expressed as [24, 25]

$$G_{i_d}(s) = \frac{V_{bus}(sC_0 + (2/R_{Load}))}{L_1 C_0 s^2 + (L_1/R_{Load})s + 2D'^2}, \quad (11)$$

where D' is a coefficient.

3. Control Strategy

Based on the previously described model of the three-phase bidirectional grid-connected AC/DC converter with L filter, this section has introduced the converter control strategy. The DC bus voltage of the V2G system is the main control object. Therefore, the most widely used control strategy, the voltage outer-loop, and current inner-loop double PI control are applied in this paper. So as to improve the stability of the system, the grid voltage feedforward decoupling scheme is used.

3.1. Grid Voltage Feedforward Decoupling Scheme. Obviously, cross-coupling term is in synchronous $d-q$ frame from the previously described model. In order to control the d -axis and q -axis current independently, decoupling method is used frequently. And the output also will be turbulent by the grid voltage. So, the grid voltage feedforward decoupling scheme is applied to the converter.

From (9), the model of synchronous $d-q$ frame can be described as the following equation, when $u_d = S_d u_{dc}$ and $u_q = S_q u_{dc}$ [26]:

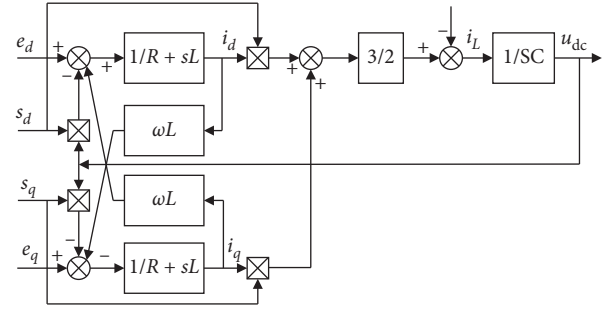


FIGURE 3: The model of three-phase converter in synchronous $d-q$ frame.

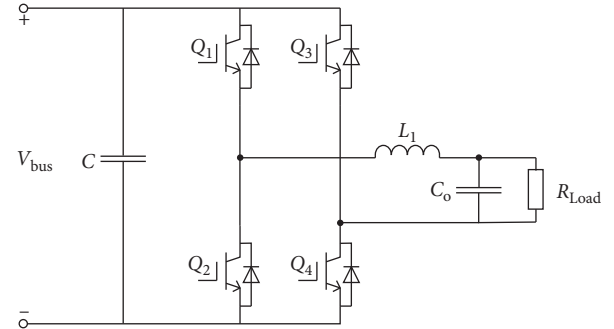


FIGURE 4: The topology of bidirectional DC/DC converter.

$$\begin{cases} u_d = e_d - L \frac{di_d}{dt} + \omega_0 Li_q - Ri_d, \\ u_q = e_q - L \frac{di_q}{dt} - \omega_0 Li_d - Ri_q. \end{cases} \quad (12)$$

It can be confirmed that adjusting i_d and i_q can obtain the AC-side voltage u_d and u_q . Define the reference u_d^* and u_q^* as [26]

$$\begin{cases} u_d^* = L \frac{di_d}{dt} + Ri_d, \\ u_q^* = L \frac{di_q}{dt} + Ri_q. \end{cases} \quad (13)$$

The injected grid current can be described as (14) according to (13). And u_d and u_q are obtained as (15), when the PI regulator is used [26]:

$$\begin{cases} i_d(s) = \frac{1}{sL + R} u_d^*(s), \\ i_q(s) = \frac{1}{sL + R} u_q^*(s), \end{cases} \quad (14)$$

$$\begin{cases} u_d = e_d + \omega_0 Li_q - \left(K_P + \frac{K_I}{s}\right)(i_d^* - i_d), \\ u_q = e_q + \omega_0 Li_d - \left(K_P + \frac{K_I}{s}\right)(i_q^* - i_q), \end{cases} \quad (15)$$

where i_d^* and i_q^* are the reference current of d -axis and q -axis, respectively. K_p and K_I are the proportional and integration coefficients. From (15), the control diagram of feedforward decoupling is shown in Figure 5 [26, 27].

Applying (15) to (12), the model in $d-q$ frame is obtained as [26]

$$\begin{cases} \frac{di_d}{dt} = -\frac{1}{L} \left[R + \left(K_p + \frac{K_I}{s} \right) \right] i_d + \frac{1}{L} \left(K_p + \frac{K_I}{s} \right) i_d^*, \\ \frac{di_q}{dt} = -\frac{1}{L} \left[R + \left(K_p + \frac{K_I}{s} \right) \right] i_q + \frac{1}{L} \left(K_p + \frac{K_I}{s} \right) i_q^*. \end{cases} \quad (16)$$

From (16), there are no cross-coupling terms and grid voltage effects. Figure 6 shows the current loop control diagram of grid voltage feedforward decoupling.

In this paper, i_q^* and i_d^* are set to control the system reactive power and active power. The system is operating at unit power factor, so i_q^* is set to 0.

3.2. Current Closed-Loop Design. The inner current closed loop is used to keep the sinusoidal current input for system. It is obvious that the i_d and i_q current loops are similar and symmetrical. Taking the i_d current loop as an example, the decoupling control diagram of d -axis current loop is shown in Figure 7. T_s is the sample period of current loop; K_{iP} and K_{iI} are the proportional and integration coefficients of PI regulator, respectively; and K_{pwm} is the equivalent gain of the three-phase pulse width modulated converter. In this paper, SVPWM modulation is applied, so K_{pwm} is 1. Ignoring the grid voltage effects, the simplified inner current loop diagram can be described as in Figure 8 [28].

τ_i can be expressed as [28]

$$\tau_i = \frac{K_{iP}}{K_{iI}}. \quad (17)$$

The current open-loop transfer function is [28]

$$G_{oi}(s) = \frac{K_{iP}K_{pwm}}{R\tau_i s (1.5T_s s + 1)}. \quad (18)$$

When $\zeta = 0.707$, it can be derived that [28]

$$\frac{1.5T_s K_{iP} K_{pwm}}{R\tau_i} = \frac{1}{2}. \quad (19)$$

Considering (18) and (19), the parameter of current loop can be calculated as follows [28]:

$$\begin{cases} K_{iP} = \frac{R\tau_i}{3T_s K_{pwm}}, \\ K_{iI} = \frac{K_{iP}}{\tau_i} = \frac{R}{3T_s K_{pwm}}. \end{cases} \quad (20)$$

Similarly, the current closed-loop transfer function can be derived from open-loop transfer function, which can be expressed as

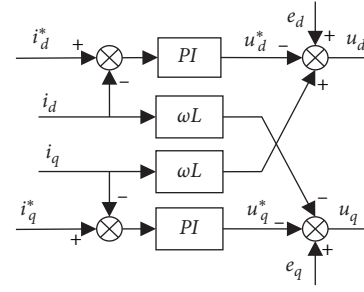


FIGURE 5: Control diagram of feedforward decoupling.

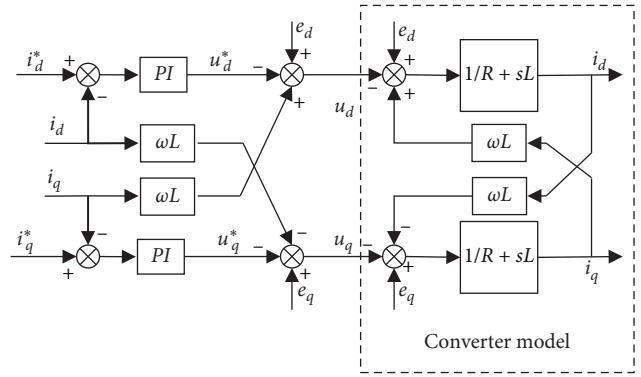


FIGURE 6: Current loop control diagram of grid voltage feedforward decoupling.

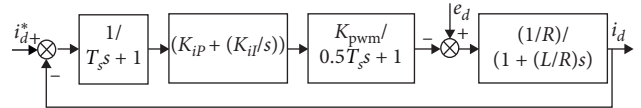


FIGURE 7: The control diagram of inner current loop.

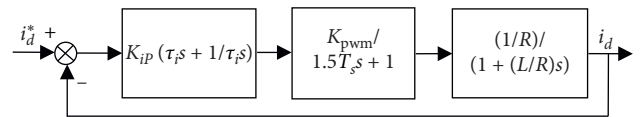


FIGURE 8: The simplified control diagram of inner current loop.

$$G_{ci}(s) = \frac{1}{1 + (R\tau_i/K_{iP}K_{pwm})s + (1.5T_s R\tau_i/K_{iP}K_{pwm})s^2}. \quad (21)$$

When the system switching frequency is high enough, it means that T_s is small enough. s^2 can be omitted. Thus, the current closed-loop transfer function can be simplified as

$$G_{ci}(s) \approx \frac{1}{1 + (R\tau_i/K_{iP}K_{pwm})s}. \quad (22)$$

Comparing (20) and (22), $G_{ci}(s)$ can be simplified to

$$G_{ci}(s) = \frac{1}{1 + 3T_s s}. \quad (23)$$

From (23), the current loop can be equivalent to a first-order inertial element, where $3T_s$ is inertial time constant. It can be concluded that the system current loop has fast dynamic response in high switch frequency.

3.3. Voltage Closed-Loop Design. The voltage closed loop can keep the DC bus voltage stable and provide reference values for the current closed loop. Considering the simplified current close-loop transfer function, the voltage closed-loop diagram is shown in Figure 9. τ_v is the inertial time constant of voltage closed loop; K_v and T_v are the PI parameters of voltage loop; and $G_{ci}(s)$ is the current loop transfer function. K can be expressed as [28]

$$0.75 m \cos \theta \leq 1, \quad (24)$$

where m is the PWM modulation ratio and θ is the initial phase.

In Figure 9, K is time variable, which is not convenient for system design. Because the max PWM modulation ratio is 1, it is obvious that the $0.75m \cos \theta \leq 1$. So, it can be replaced by a constant 0.75. At the same time, substituting the current loop transfer function, the simplified diagram of voltage closed loop is shown in Figure 10.

The voltage open-loop transfer function can be expressed as [28]

$$G_{ov}(s) = \frac{0.75K_v(T_v s + 1)}{CT_v s^2(T_{ev} s + 1)}, \quad (25)$$

where $T_{ev} = \tau_v + 3T_s$. Then, the voltage closed-loop transfer function can be expressed as

$$G_{cv} = \frac{1}{1 + (CT_v s^2(T_{ev} s + 1)/0.75K_v(T_v s + 1))}. \quad (26)$$

The intermediate-frequency bandwidth of the voltage loop is defined as [29]

$$h_v = \frac{T_v}{T_{ev}}. \quad (27)$$

According to the principles of the typical II system [29, 30], it can be expressed as

$$\frac{0.75K_v}{CT_v} = \frac{h_v + 1}{2h_v^2 T_{ev}^2}. \quad (28)$$

Considering the immunity and followability of the voltage loop, h_v is generally set as 5. After substitution and calculation, the parameters of voltage loop are

$$\begin{cases} T_v = 5T_{ev} = 5(\tau_v + 3T_s), \\ K_v = \frac{4C}{(\tau_v + 3T_s)}. \end{cases} \quad (29)$$

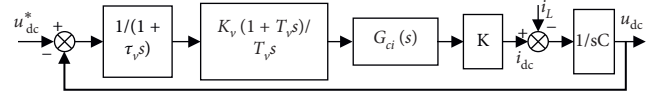


FIGURE 9: The control diagram of voltage closed loop.

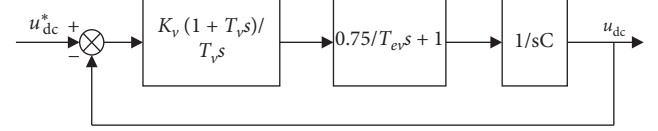


FIGURE 10: The simplified control diagram of voltage closed loop.

4. Simulation and Experiment Results

4.1. Simulation Results. An 80 kW V2G system simulation model is established in MATLAB/Simulink. The control schemes mentioned above are applied to the AC/DC converter. And the single current closed loop is used in bidirectional DC/DC converter. System configuration is shown in Figure 1, and the detailed parameters of the converter are shown in Table 1.

The system Bode diagrams are shown in Figure 11. The proportional and integration coefficients of current PI regulator have been obtained as 2, 200, respectively, as shown in Figure 11(a). And the values of $K_v = 4$, $K_v/T_v = 45$ have been selected for voltage PI regulator shown in Figure 11(b).

Figure 12 shows the converter output DC voltage waveforms with zero load. The initial voltage of converter is 570 V, and the output reference voltage is 800 V. After about 0.1 s, the output voltage is 800 V. The overshoot voltage of system is about 20 V, and the output ripple voltage is about 1 V.

Figure 13 shows the dynamic performance of three-phase bidirectional grid-connected converter. The load steps from 0 to full load, when time = 0.01s.

From Figure 13(a), u_{dc} drops from 800V to 747.1 V at time = 0.01 s. Then, the voltage returns to original output, which takes about 140.2 ms, and the ripple is about 1.8 V. Grid-connected currents i_a, i_b, i_c are shown in Figure 13(b). The currents increase at time = 0.01 s and eventually stabilize at 99.77 A RMS. The Fourier analysis of grid-connected current shows that THD of the grid current is about 2.3%.

Through comparing u_{dc} and i_a, i_b, i_c in Figure 13, it can be concluded that the proposed AC/DC converter works with a balanced and low THD three-phase grid-connected current, and it performs fast DC voltage regulation under full load disturbances.

Figure 14 shows the simulation results of the V2G system in charging and discharging. From time = 0 s to time = 0.25 s, the power flow of the system is negative, which indicates that the battery is discharging. From time = 0.25 s to time = 0.5 s, the power flow is positive, which indicates that the battery is charging. And the power of charge and discharge is 80 kW.

From Figure 14(a), u_{dc} increases from 800 V to 837.6 V at the beginning of discharging. After about 175.37 ms, u_{dc}

TABLE 1: System parameters.

Symbol	Parameters	Value (V)
e_a, e_b, e_c	Grid voltage (RMS)	220
L	Grid-side filter inductance	0.9
R	Resistor	0.1
C	DC-bus filter capacitor	12000
L_1	DC inductance	0.2
C_o	DC capacitor	2000
u_{dc}	DC-bus voltage	800
u_{bat}	Battery voltage	500
f_s	Switching frequency	10
f_{line}	Grid frequency	50

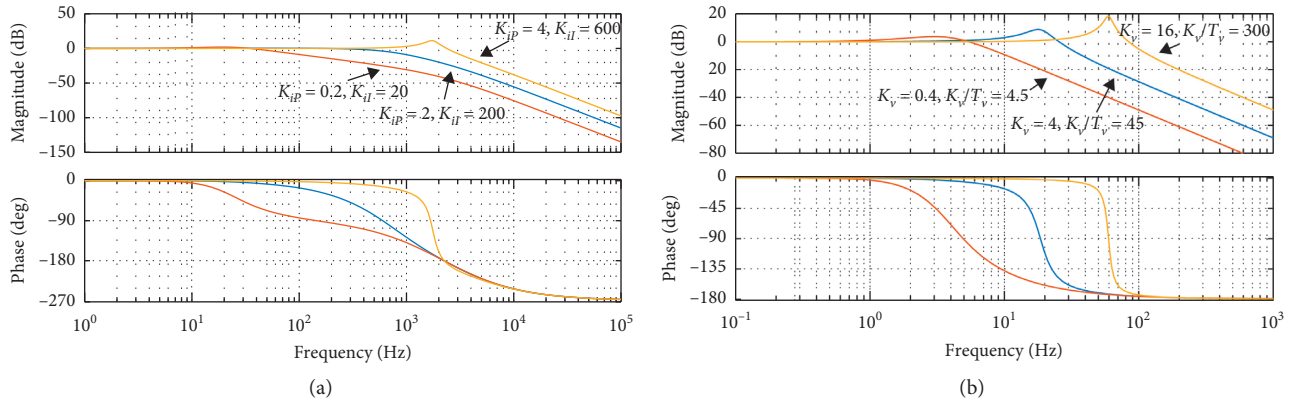


FIGURE 11: The Bode diagram of system. (a) Bode diagram of current closed loop in the case of different values for the proportional and integration coefficients (21). (b) Bode diagram of voltage closed loop in the case of different values for the proportional and integration coefficients (26).

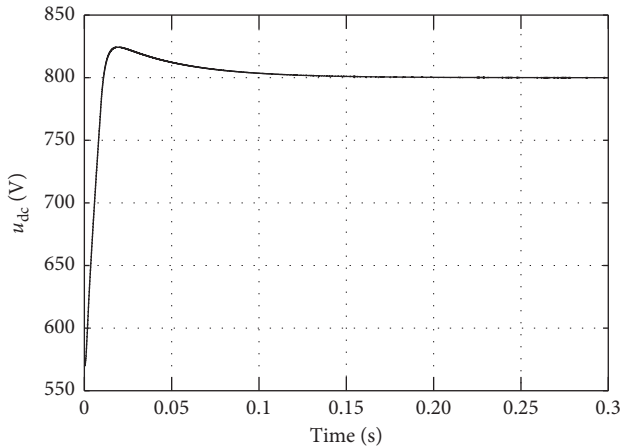


FIGURE 12: The DC bus voltage waveform of AC/DC converter without load.

restored to original output and the ripple is about 2 V. u_{dc} drops from 800 V to 722.5 V, when the power flow changes at time = 0.25 s. After about 200.25 ms, the voltage restored to original output. Figure 14(b) shows the battery State of Charge (SOC). From time = 0 s to time = 0.25 s, the battery is discharging. After time = 0.25 s, the battery is charging. Figures 14(c) and 14(d) depict the phase A grid-connected current and voltage. It can be observed that i_a and e_a are the

same frequency but opposite phase, when time < 0.25 s. And i_a and e_a are the same frequency and phase, when time > 0.25 s. The current THD is 3.5%, while the battery is discharging. And the current THD is 2.23%, while the battery is charging.

The simulation results show the correctness of design in terms of high-power factor, low current harmonic distortion, and constant output voltage.

4.2. Experiment Results. An 80 kW prototype is built and tested in lab, as shown in Figure 15. The AC/DC converter and DC/DC converter are both evaluated. The battery is replaced by a grid-connected converter. Table 1 shows the key parameters of system. The controller is DSP (TMS320F28335) and FPGA (XC6SLX9). The IGBT is Infineon FF450R12KT4, and the driver of IGBT is CONCEPT 2SC0435.

Figure 16 shows the converter waveforms in different conditions. The DC bus voltage u_{dc} and grid-connected current i_a are shown in Figure 16(a) when the converter output with full load in charging. The u_{dc} is 800 V and the ripple is about 3 V. Fourier analysis is made for i_a ; the THD of current is 1.1%. The step response waveforms are shown in Figure 16(b). It can be observed that the reference steps from 0 to full load, when time = 0.0 s. DC bus voltage drops from 800 V to 769.8 V and returns to original output, after about

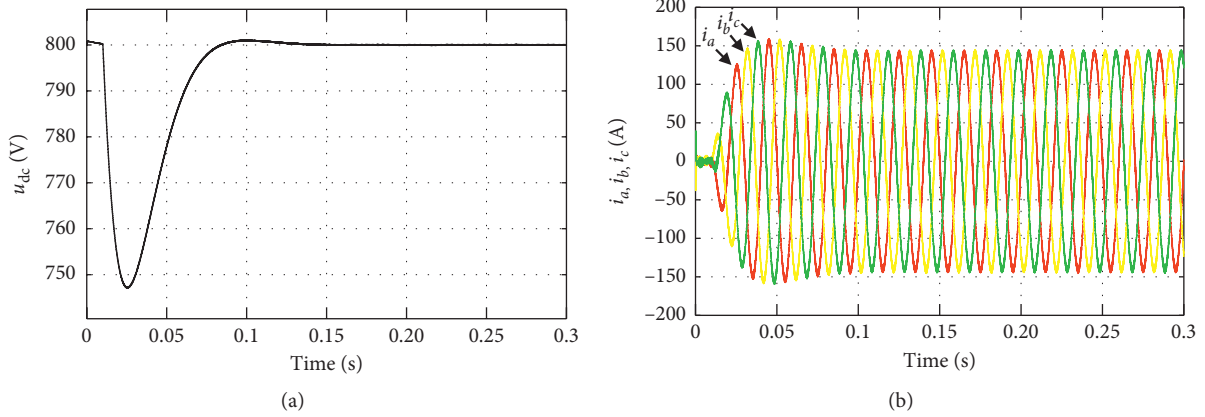


FIGURE 13: Step response of converter. (a) The step response of AC/DC converter DC bus voltage. (b) The step response of AC/DC converter grid-connected current.

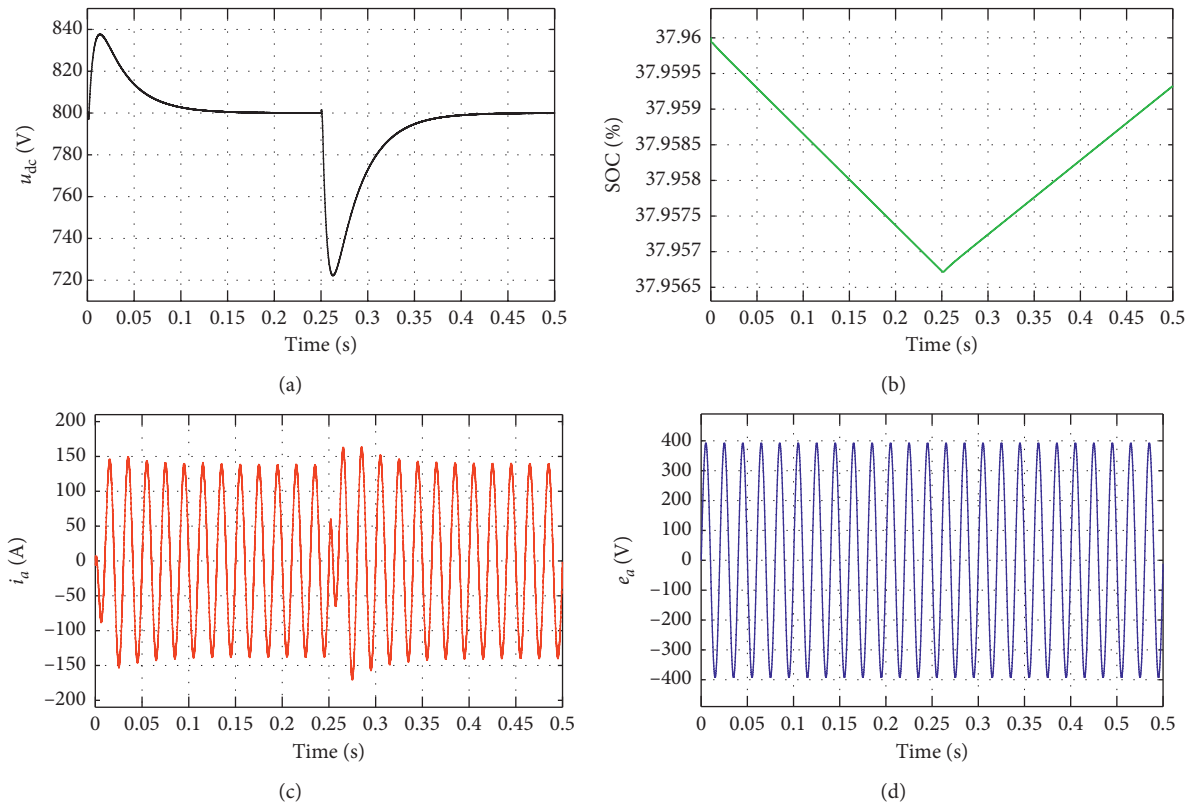


FIGURE 14: The waveforms of V2G system in different conditions. (a) The DC bus voltage of bidirectional AC/DC converter. (b) The state of charge (SOC) of battery. (c) The grid-connected current curve of phase A. (d) The grid voltage curve of phase A.

178.8 ms. The system performs well in step response and full load with designed control schemes and parameters.

From Figure 16(c), before power flow reverse, the battery is charging, which means that the bidirectional AC/DC converter works under rectifier state, and the phase current THD is 1.1%. After power flow reverse, the battery is discharging, which represents that the bidirectional AC/DC converter works in inverter state. And the phase current

THD is 2.1%. Before the power flow changes, the DC-bus voltage is 800V. When the power flow changes, the voltage increased about 65 V and restored to the original output voltage after 260.5 ms. From Figure 16(d), in charging, i_a and e_a are at the same frequency and phase. On the contrary, in discharging, the current and voltage are at the same frequency but opposite phase. As a result, the converter is stable and works well in the power flow reverse condition.

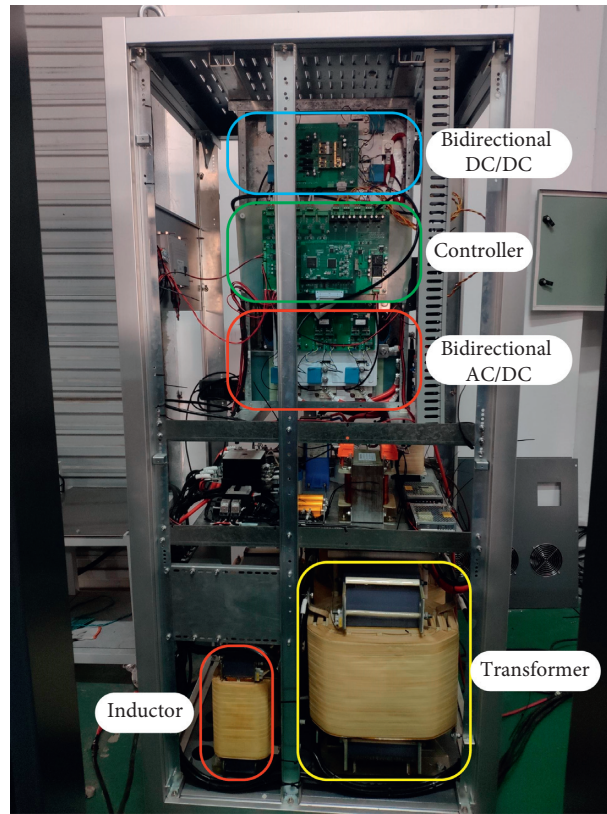


FIGURE 15: The photo of experiment platform.

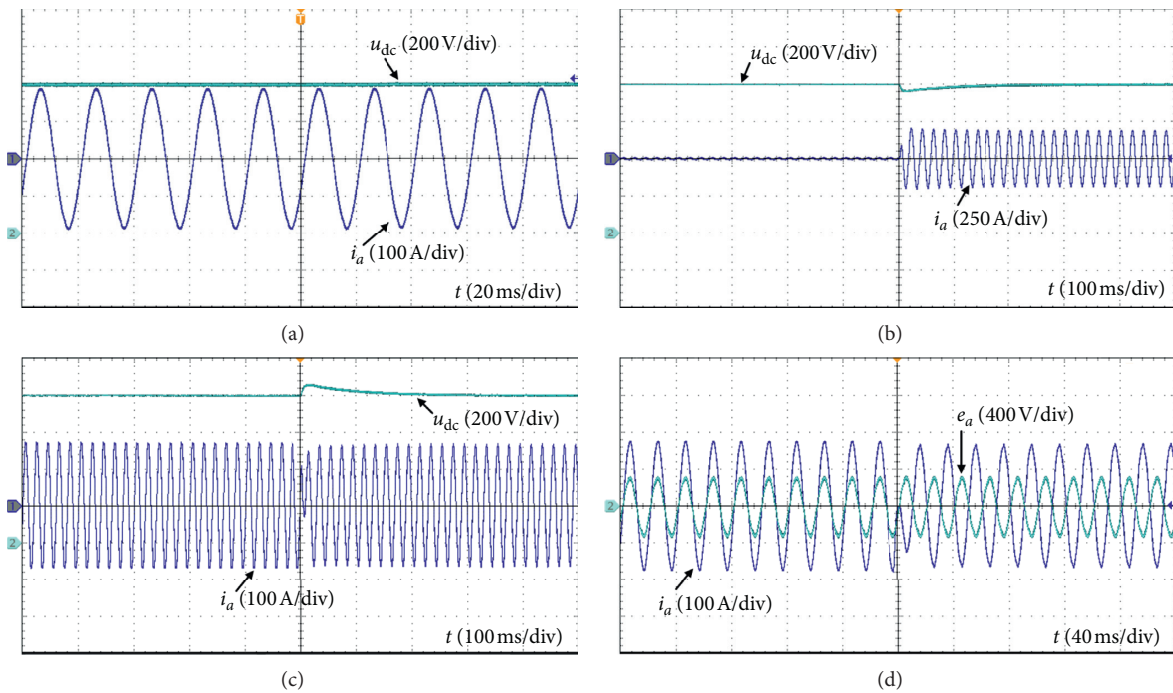


FIGURE 16: The waveforms of bidirectional AC/DC converters. (a) The grid-connected current and DC bus voltage of converter in full load condition. (b) The DC voltage and grid-connected current of converter in step response. (c) The DC bus voltage and grid-connected current of converter in power flow reverse condition. (d) The grid voltage and grid-connected current of converter in power flow reverse condition.

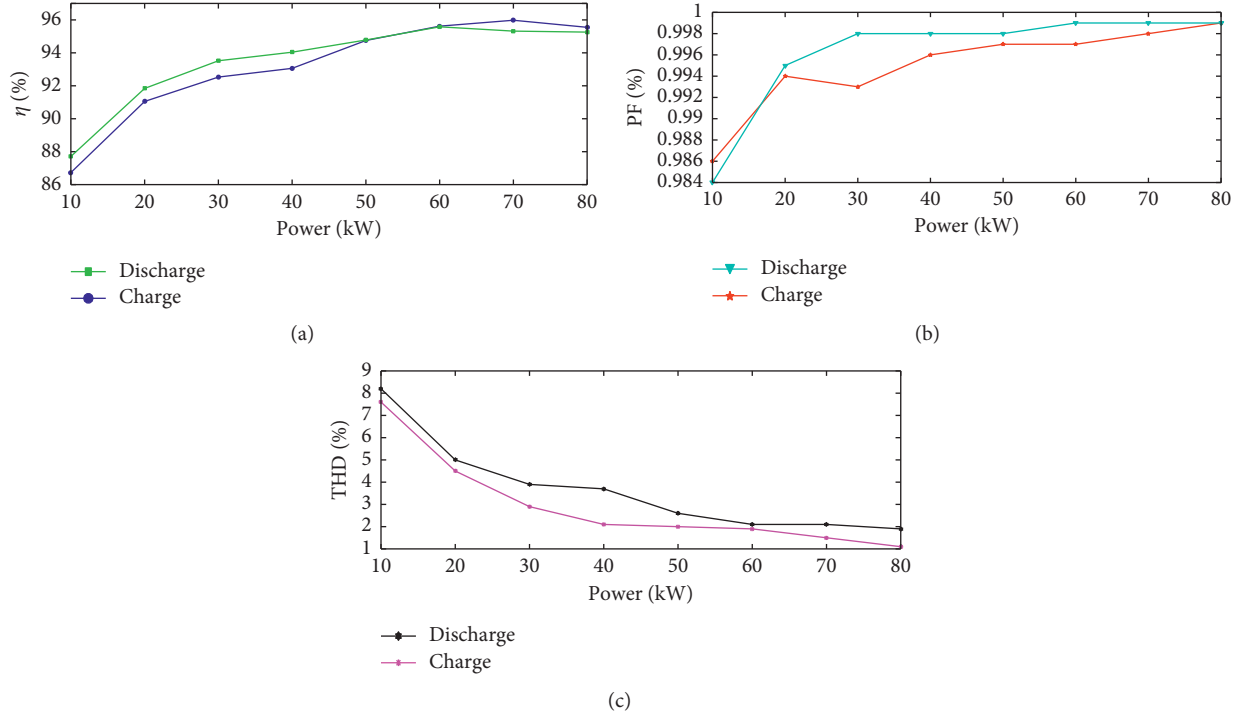


FIGURE 17: The curve of converter under different load conditions. (a) The efficiency curve. (b) The power factor curve. (c) THD curve.

The experiment results presented here further demonstrate the effectiveness of the converter proposed in this paper.

As shown in Figure 17(a), the lowest efficiency is 86.73% with 10 kW load, and the highest efficiency is 95.98% in charge mode; the lowest and highest efficiency are, respectively, 87.71% and 95.55% in discharge mode.

Figure 17(b) gives the converter power factor curve in charge state and discharge state. In charging, the lowest and highest power factors are 0.986 and 0.999, respectively. In discharging, the lowest and highest power factors are 0.984 and 0.999, respectively. From Figure 17(b), it can be shown that the converter has a unit power factor.

Figure 17(c) shows the THD of the converter. Obviously, in charging, the THD is less than 5% when the converter output power is more than 20 kW. And the lowest THD is 1.1% with full load. In discharging, the THD is less than 5% when the battery output power is more than 23 kW. And the lowest THD is 1.9% with full load. Therefore, the converter grid-connected current is low THD.

Unfortunately, both in charge and discharge modes, the efficiency, and current THD of the converter are not very good with less than 20 kW. But, under other power condition, the converter works well. It also can be concluded that the AC/DC converter and control method can be applied to the V2G system.

5. Conclusions

A three-phase bidirectional grid-connected AC/DC converter for V2G system is presented in this paper. And the mathematic model of three-phase AC/DC converter in the synchronous $d-q$ frame is built. Since the grid current will

be affected by the grid voltage distortion and the cross-coupling terms, the feedforward scheme of grid voltage is applied to the bidirectional AC/DC converter in the synchronous $d-q$ frame. And the PI controllers of voltage and current closed loop for the converter are designed. Finally, the model is established in MATLAB/Simulink, and the experimental prototype is built in lab. Simulation and experiment results show that the converter works well for V2G application with unity power factor, low voltage ripple, high efficiency, and low current THD.

Abbreviations

u_{dc}, i_{dc} :	DC voltage and current of AC/DC converter
u_{dc}^* :	Reference value of AC/DC converter DC voltage
u_{bat}, i_{bat} :	Battery voltage and current
i_{bat}^* :	Reference value of battery current
e_a, e_b, e_c :	Grid phase voltage
i_a, i_b, i_c :	Grid phase current
L, R :	Grid inductance filter and its equivalent resistor
C :	DC-bus filter capacitor
i_L :	Load current of AC/DC converter
R_L, e_L :	DC load and DC electromotive force
S_k :	Switching function of IGBT switches
x_α, x_β :	Stationary $\alpha-\beta$ frame quantities
M :	Transformation matrix of $a-b-c$ to $\alpha-\beta$.
e_α :	Frame components of voltage
e_β :	Frame components of voltage
i_α :	Frame current
i_β :	Frame current
ω_0, ω :	Rotation angular velocity of $d-q$ frame and angular velocity of grid
x_d, x_q :	Synchronous $d-q$ frame quantities

T :	Transformation matrix of $\alpha - \beta$ to $d - q$
e_d ,	Frame components of voltage
$e_q d - q$:	
i_d ,	Frame current
$i_q d - q$:	
V_{bus} :	Input voltage of DC/DC converter
C_o :	Output capacitor of DC/DC converter
L_1 :	Output inductor of DC/DC converter
R_{Load} :	Load of DC/DC converter
Dl :	Coefficient of DC/DC converter
i_d^* , i_q^* :	Reference value of i_d and i_q
K_p , K_i :	Proportional and integration coefficient of PI regulator
T_s :	Sample period of system
K_{ip} , K_{il} :	PI parameters of current controller
K_{pwm} :	Equivalent gain of the three-phase pulse width modulated converter
τ_i , τ_v :	Inertial time constant of voltage and current closed loop
K_v , T_v :	PI parameters of voltage loop
m :	PWM modulation ratio
θ :	Initial phase of grid
h_v :	Intermediate-frequency bandwidth of the voltage loop.

Data Availability

The data used to support the findings of this study are available from the corresponding author upon request.

Conflicts of Interest

The authors declare that they have no conflicts of interest regarding the publication of this paper.

Acknowledgments

This work was supported in part by the National Natural Science Foundation of China under Grant no. 61673260.

References

- [1] S. Habib, M. M. Khan, F. Abbas, L. Sang, M. U. Shahid, and H. Tang, "A comprehensive study of implemented international standards, technical challenges, impacts and prospects for electric vehicles," *IEEE Access*, vol. 6, pp. 13866–13890, 2018.
- [2] S. Esther, S. K. Singh, A. K. Goswami et al., "Recent challenges in vehicle to grid integrated renewable energy system: a review," in *Proceedings of the 2018 Second International Conference on Intelligent Computing and Control Systems (ICICCS)*, pp. 427–435, Madurai, India, 2018.
- [3] P. K. Joseph, E. Devaraj, and A. Gopal, "Overview of wireless charging and vehicle-to-grid integration of electric vehicles using renewable energy for sustainable transportation," *IET Power Electronics*, vol. 12, no. 4, pp. 627–638, 2019.
- [4] M. A. Masrur, A. G. Skowronska, J. Hancock et al., "Military-based vehicle-to-grid and vehicle-to-vehicle microgrid-system Architecture and implementation," *IEEE Transactions on Transportation Electrification*, vol. 4, no. 1, pp. 157–171, 2018.
- [5] B. Sah, P. Kumar, R. Rayudu, S. K. Bose, and K. P. Inala, "Impact of sampling in the operation of vehicle to grid and its mitigation," *IEEE Transactions on Industrial Informatics*, vol. 15, no. 7, pp. 3923–3933, 2019.
- [6] T. Chen, X.-P. Zhang, J. Wang et al., "A review on electric vehicle charging infrastructure development in the UK," *Journal of Modern Power Systems and Clean Energy*, vol. 8, no. 2, pp. 193–205, 2020.
- [7] S. I. Vagropoulos, G. A. Balaskas, and A. G. Bakirtzis, "An investigation of plug-in electric vehicle charging impact on power systems scheduling and energy costs," *IEEE Transactions on Power Systems*, vol. 32, no. 3, pp. 1902–1912, 2017.
- [8] A. Sridhar and A. R. Prabu, *Bidirectional AC-DC Converter for Vehicle-To-Grid (V2G) Applications*, Marquette University, Milwaukee, WI, USA, 2015.
- [9] S. Liu, D. Xin, and L. Yang, "A novel single-phase bidirectional electric-drive-reconstructed onboard converter for electric vehicles," *IEEE Access*, vol. 8, pp. 44739–44747, 2020.
- [10] J. Zhang, H. Yan, N. Ding et al., "Electric vehicle charging network development characteristics and policy suggestions," in *Proceedings of the 2018 International Symposium on Computer, Consumer and Control (IS3C)*, pp. 469–472, Taichung, China, 2018.
- [11] B. Koushki, P. Jain, and A. Bakhshai, "Topology and controller of an isolated bi-directional AC-DC converter for electric vehicle," in *Proceedings of the 2016 IEEE Energy Conversion Congress and Exposition (ECCE)*, pp. 1–8, Milwaukee, WI, USA, 2016.
- [12] K. V. Sing, H. O. Bansal, and D. Singh, "A comprehensive review on hybrid electric vehicles: architectures and components," *Journal of Modern Transportation*, vol. 27, no. 2, pp. 77–107, 2019.
- [13] P. Yang, T. Peng, H. Wang et al., "A single-phase current-source bidirectional converter for V2G application," in *Proceedings of the 2017 IEEE 3rd International Future Energy Electronics Conference and ECCE Asia (IFEEC 2017-ECCE Asia)*, pp. 704–709, Kaohsiung, Taiwan, 2017.
- [14] A. K. Singh and M. K. Pathak, "Single-phase bidirectional ac/dc converter for plug-in electric vehicles with reduced conduction losses," *IET Power Electronics*, vol. 11, no. 1, pp. 140–148, 2018.
- [15] B. Singh and R. Kushwaha, "A PFC based EV battery charger using a bridgeless isolated SEPIC converter," *IEEE Transactions on Industry Applications*, vol. 56, no. 1, pp. 477–487, 2020.
- [16] M. R. T. Hossain, A. H. Abedin, and M. A. Choudhury, "A single phase SEPIC AC-DC Converter with improved power factor and input current THD," in *Proceedings of the 2016 9th International Conference on Electrical and Computer Engineering (ICECE)*, pp. 373–376, Dhaka, Bangladesh, 2016.
- [17] T.-L. Nguyen and H.-H. Lee, "An enhanced control strategy for AC-DC matrix converters under unbalanced grid voltage," *IEEE Transactions on Industrial Electronics*, vol. 67, no. 3, pp. 1718–1727, 2020.
- [18] D. Mishra, B. Singh, and B. K. Panigrahi, "Adaptive current control for a Bi-directional interleaved EV charger with disturbance rejection," in *Proceedings of the 2020 IEEE International Conference on Power Electronics, Smart Grid and Renewable Energy (PESGRE2020)*, Cochin, India, pp. 1–6, 2020.
- [19] J. Zhao and Q. Jiang, "Research on a new control strategy for three-phase current-source PWM rectifier," in *Proceedings of the 2017 Eighth International Conference on Intelligent Control and Information Processing (ICICIP)*, pp. 157–161, Hangzhou, China, 2017.

- [20] O. Noureldeen, I. Hamdan, and B. Hassanin, "Design of advanced artificial intelligence protection technique based on low voltage ride-through grid code for large-scale wind farm generators: a case study in Egypt," *SN Applied Sciences*, vol. 1, no. 6, pp. 1–19, 2019.
- [21] O. Noureldeen and I. Hamdan, "Design of robust intelligent protection technique for large-scale grid-connected wind farm," *Protection and Control of Modern Power Systems*, vol. 3, no. 1, pp. 1–13, 2018.
- [22] K. Qian, G. Gao, and Z. Sheng, "A maximum current control method for three-phase PWM rectifier for the ITER in-vessel vertical stability coil power supply," *IEEE Transactions on Plasma Science*, vol. 46, no. 5, pp. 1689–1693, 2018.
- [23] W. Li, X. Ruan, D. Pan, and X. Wang, "Full-feedforward schemes of grid voltages for a three-phase LCL-Type grid-connected inverter," *IEEE Transactions on Industrial Electronics*, vol. 60, no. 6, pp. 2237–2250, 2013.
- [24] Z. Tao and L. Li, "Control loop design and bidirectional control strategy of a bidirectional DC/DC converter," in *Proceedings of the 2017-43rd Annual Conference of the IEEE Industrial Electronics Society (IECON)*, pp. 5720–5725, Beijing, China, 2017.
- [25] A. AlZawaideh and I. Boiko, "Analysis of a sliding mode DC-DC boost converter through LPRS of a nonlinear plant," *IEEE Transactions on Power Electronics*, vol. 35, no. 11, pp. 12321–12331, 2020.
- [26] Q. Yan, X. Wu, X. Yuan, and Y. Geng, "An improved grid-voltage feedforward strategy for high-power three-phase grid-connected inverters based on the simplified repetitive predictor," *IEEE Transactions on Power Electronics*, vol. 31, no. 5, pp. 3880–3897, 2016.
- [27] A. F. Tazay, A. M. A. Ibrahim, O. Noureldeen, and I. Hamdan, "Modeling, control, and performance evaluation of grid-tied hybrid PV/wind power generation system: case study of gabel el-zeit region, Egypt," *IEEE Access*, vol. 8, pp. 96528–96542, 2020.
- [28] C. Lu, S. Yang, X. Wei et al., "Research on the technology of the neutral-point voltage balance and dual-loop control scheme for three-level PWM inverter," in *Proceedings of the 2012 Asia-Pacific Power and Energy Engineering Conference (APPEEC)*, pp. 1–4, Shanghai, China, 2012.
- [29] P. Yang and L. Deng, *Parameter Tuning Method and Application of PID Controller*, pp. 9–19, China Electric Power Publishing Press, Beijing, China, 2016.
- [30] L. Yang and J. Yang, "A robust dual-loop current control method with a delay-compensation control link for LCL-type shunt active power filters," *IEEE Transactions on Power Electronics*, vol. 34, no. 7, pp. 6183–6199, 2019.